Multistage strain hardening through dislocation substructure and twinning in a high strength and ductile weight-reduced Fe–Mn–Al–C steel

I. Gutierrez-Urrutia *, D. Raabe

Max-Planck-Institut für Eisenforschung, Max-Planck Str. 1, D-40237 Düsseldorf, Germany

Abstract

We investigate the kinetics of the deformation structure evolution and its contribution to the strain hardening of a Fe–30.5Mn–2.1Al–1.2C (wt.%) steel during tensile deformation by means of transmission electron microscopy and electron channeling contrast imaging combined with electron backscatter diffraction. The alloy exhibits a superior combination of strength and ductility (ultimate tensile strength of 1.6 GPa and elongation to failure of 55%) due to the multiple-stage strain hardening. We explain this behavior in terms of dislocation substructure refinement and subsequent activation of deformation twinning. The early hardening stage is fully determined by the size of the dislocation substructure, namely, Taylor lattices, cell blocks and dislocation cells. The high carbon content in solid solution has a pronounced effect on the evolving dislocation substructure. We attribute this effect to the reduction of the dislocation cross-slip frequency by solute carbon. With increasing applied stress, the cross-slip frequency increases. This results in a gradual transition from planar (Taylor lattices) to wavy (cells, cell blocks) dislocation configurations. The size of such dislocation substructures scales inversely with the applied resolved stress. We do not observe the so-called microband-induced plasticity effect. In the present case, due to texture effects, microbanding is not favored during tensile deformation and, hence, has no effect on strain hardening.
© 2012 Acta Materialia Inc. Published by Elsevier Ltd. All rights reserved.

Keywords: Strain hardening; Electron channeling contrast imaging; Austenitic steel; Deformation structures; Dislocation structures

1. Introduction

High manganese steels have an outstanding combination of strength and ductility owing to their high strain hardening capacity. They are austenitic, i.e. face-centered cubic (fcc) alloys, with a high Mn content (typically between 20 and 30 wt.%) and additions of elements such as carbon (<1 wt.%), silicon (<3 wt.%), or aluminum (<10 wt.%) [1–11]. High-Mn steels exhibit different hardening mechanisms which have been commonly interpreted in terms of the stacking fault energy [6,8,9,12–18]. Several authors have considered the role of clustering of carbon and manganese atoms on strain hardening [5,19–21], in particular, on the occurrence of serrated flow. For instance, Saeed-Akbari et al. [22] have recently addressed the influence of short range ordering (SRO) on strain hardening. These authors suggest a strain hardening parameter (the so-called theoretical ordering index, TOI) that is related to the SRO strengthening mechanism. Among the different strain hardening mechanisms, twinning-induced plasticity (TWIP) has received much interest due to the good mechanical compatibility between dislocation slip and the dynamically refined twin interfaces compared to other chemical/crystallographic interfaces (for instance, ε-martensite) [1,4,6–8,13,23,24]. As twin interfaces act as strong obstacles to dislocation glide, microstructure refinement by deformation twinning increases the strain-hardening rate. The TWIP effect is therefore determined by the twinning kinetics, more specifically by the twinning rate and the average twin spacing.

* Corresponding author. Tel.: +49 2116792 407; fax: +49 2115792333.
E-mail address: i.gutierrez@mpie.de (I. Gutierrez-Urrutia).

Recently, a new hardening mechanism has been proposed in high-Mn steels, namely, microband-induced plasticity (MBIP) [3,25,26]. This mechanism has been reported in Fe–Mn–Al–C alloys with high stacking fault energy (50–90 mJ m^{-2}). These alloys exhibit an outstanding combination of strength (ultimate tensile strength of ~900 MPa) and ductility (~100% elongation to fracture). Furthermore, the high aluminum content (up to 10 wt.%) renders these steels lightweight alternatives to conventional high strength structural materials. MBIP has been ascribed to the formation of microbands and their role as an individual strain hardening mechanism. The microbands were described as in-grain narrow shear zones that are delimited by geometrically necessary boundaries. However, upon deformation different types of dislocation substructures such as highly dense dislocation walls (HDDWs) and Taylor lattices have been observed as well. Up to now no detailed quantitative characterization of the underlying kinetics of the substructure evolution and their correspondence to the stress–strain and strain hardening evolution in the FeMnAlC system have been performed. Specifically, the contributions of the different types of dislocation substructures, namely, HDDWs, Taylor lattices and microbands, to the excellent strain hardening capacity of FeMnAlC steels are still unclear. Therefore, the present study has the following aims. First, we study in detail the contribution of the evolving dislocation substructure and its effect on strain hardening. Specifically, we aim at clarifying the role of microbanding in FeMnAlC steels. Second, we explore the various suggested strain hardening mechanisms, namely, microband hardening through dislocation substructure pattering (MBIP) and deformation twinning (TWIP), as well as their interactions, in order to better understand the strain hardening behavior of FeMnAlC steels. For these purposes, we have selected a Fe–30.5Mn–2.1Al–1.2C (in wt.%) alloy in solid solution state. We performed a complete quantitative characterization of the underlying deformation structure by transmission electron microscopy (TEM) and electron channeling contrast imaging (ECCI). The ECCI technique combined with electron backscatter diffraction (EBSD) allows us to characterize the deformed structure at a wide field of view in the scanning electron microscope (SEM) [4,13,23,27–30] with a better dislocation and interface contrast than the basic ECCI technique [31]. The contribution of the so characterized dislocation and twin substructures to the strain hardening is analyzed in terms of the dislocation mean free path approach.

2. Experimental

The high-Mn steel used in this study had the chemical composition Fe–30.5Mn–2.1Al–1.2C (in wt.%). The material was melted in an induction furnace under Ar atmosphere and cast to round bars of 25 mm diameter. The cast ingot was reheated to 1200 °C for 30 min, hot-rolled to 75% thickness reduction at 1100 °C, and water quenched. The hot-rolled material was then solution-trea-

ted for 2 h at 1100 °C under Ar, and final water quenching. To avoid any microstructure instability, the samples were subjected to a short annealing at 450 °C for 1 h. The as-annealed material showed a fully austenitic structure with an average grain size of 50 μm, which remained stable during deformation at room temperature. No precipitates were detected by TEM, either in diffraction mode (appearance of extra spots) or in image mode at high magnification. Hence, the present alloy was in solid solution state. Tensile tests were carried out at room temperature at an initial strain rate of 5×10^{-4} s^{-1} in a Zwick ZH 100 tensile machine. In addition to tensile testing to failure, interrupted tensile tests to true strains of $\varepsilon = 0.02$, 0.10, 0.20 and 0.30 were performed to study the microstructural evolution as a function of strain. The tensile samples were cylindrical, with gauges of 6 mm diameter and 40 mm length. Microstructures of the tensile deformed high-Mn steel were examined by EBSD, ECCI, and TEM. The longitudinal section was examined, i.e. the observation direction was perpendicular to the tensile axis. The EBSD technique was used to analyze the local crystallographic texture. Orientation maps were taken in a 6500 F JEOL field emission gun-scanning electron microscope (FEG-SEM) equipped with a TSL OIM EBSD system at 15 kV acceleration voltage and a working distance of 15 mm. Quantitative characterization of the deformed structure was conducted by ECCI, as in previous works [4,13,23,27,29,30]. We used a newly developed EBSD-based set-up to obtain ECCI images under controlled diffraction conditions, enabling enhanced dislocation and interface contrast [27]. ECCI images were obtained with optimum contrast by orienting the matrix crystal exactly in Bragg condition for a high intensity reflection and exciting the corresponding diffraction vector in a "two-beam" condition. ECCI observations were carried out in a Zeiss Crossbeam instrument (XB 1540, Carl Zeiss SMT AG, Germany). TEM observations were conducted in a Phillips CM20 microscope. Thin foil samples were prepared by electropolishing using 30% nitric acid in methanol at −30 °C and 10 V.

3. Results

3.1. Strain hardening

Fig. 1a shows the true stress–true strain curve of the Fe–30.5Mn–2.1Al–1.2C (wt.%) steel with an average grain size of 50 μm tensile deformed at an initial strain rate of 5×10^{-4} s^{-1}, i.e. the true strain rate was not constant. The material exhibits excellent mechanical properties, combining high strength (ultimate tensile strength of 1.6 GPa) and ductility (elongation to failure of 55%). At room temperature and an initial strain rate of 5×10^{-4} s^{-1}, no serrated flow occurred. The stress–strain curve exhibits a significant variation in slope at ~20% true strain. At this strain level, the slope decreases but is still positive, indicating the activation of a secondary strain hardening stage.
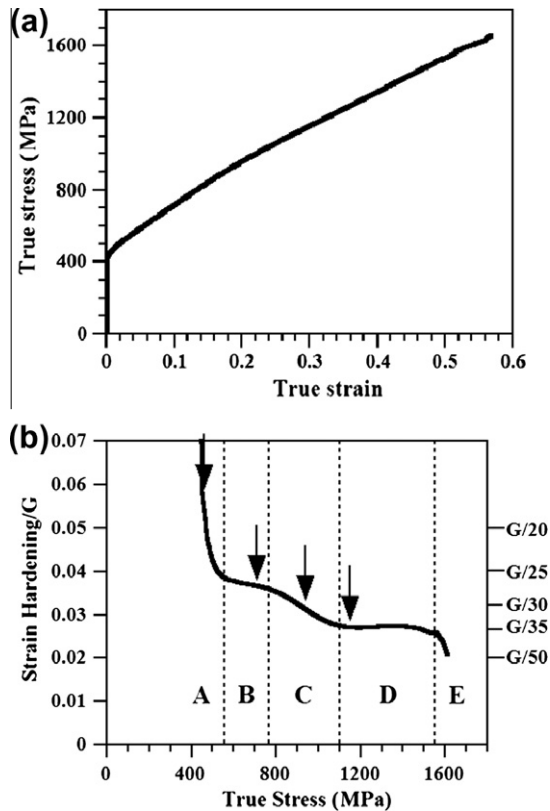
Fig. 1. True stress–true strain curve (a) and normalized strain hardening rate (normalized with shear modulus) vs. true stress (b) of Fe–30.5Mn–2.1Al–1.2C (wt.%) steel tensile deformed at an initial strain rate of $5 \times 10^{-4}\,s^{-1}$.

Fig. 1b shows the normalized strain hardening rate (normalized by the shear modulus) vs. flow stress of the tensile deformed alloy. Arrows indicate the different deformation stages described in the subsequent section. The main characteristic revealed in Fig. 1b is the occurrence of a multiple-stage strain hardening behavior. In particular, in the present material five different deformation stages can be distinguished in the evolution of the strain hardening rate with the true stress. The first stage, referred to as stage A, is characterized by a continuous decrease of the strain hardening rate until a stress of 560 MPa, stage B. This stage reveals a nearly constant hardening rate with a strain hardening coefficient of $\sim G/27$, where G is the shear modulus ($G = 70$ GPa [32]). With further stress, the strain hardening rate decreases gradually, stage C, until the onset of stage D. This stage exhibits a nearly constant strain hardening rate with a strain hardening coefficient of $\sim G/35$. Finally, the

strain hardening rate decreases until rupture, stage E. It should be pointed out that the labeling of the hardening stages used in this work must not be confused with the classical hardening stage analysis used for single crystals and polycrystals of medium–high stacking fault energy; for details see Ref. [33].

3.2. Evolution of the deformation structure

The evolution of the deformation structure is investigated at several deformation stages by TEM, EBSD and ECCI. The grain area fraction and the average size of dislocation substructures are shown in Table 1.

3.2.1. Deformation stage: 0.05 true strain/450 MPa

At this deformation stage, the slip character is planar, resulting in dislocation configurations such as pile-ups, dipole bundles, multipoles, hexagonal dislocation networks and Lomer–Cottrell locks (Figs. 2 and 3). Fig. 2a shows a weak-beam TEM image of a dipole bundle lying parallel along the $(-11-1)$ plane. The bundle consists of an array of dislocation dipoles with an average spacing of 20 nm. At this strain level, multipole configurations formed by highly ordered arrays of dipole bundles are observed, as illustrated in the weak-beam TEM image of Fig. 2b. The closed ends of the multipoles are aligned along the intersection line of the primary and cross-slip planes. In particular, the multipole configuration shown in Fig. 2b is aligned along the (-111) plane. These dislocation configurations are commonly observed in the early hardening stages of low stacking fault energy fcc metals [34–36]. The formation of such dislocation configurations, namely, dipole bundles and multipoles, involves dislocation maneuvers that require the activation of dislocation cross-slip [37].

We also observe the formation of more complex planar dislocation configurations, such as dislocation nodes, hexagonal dislocation networks and Lomer–Cottrell locks (Fig. 3). Most of the dislocation nodes observed (N: nodes, Fig. 3a), correspond to triple nodes which are formed by the interaction of dislocations gliding on coplanar systems [38]. Hexagonal dislocation networks (Fig. 3b) are generally formed by the interaction of two types of nodes, namely, extended and contracted nodes [38]. In particular, the formation of hexagonal networks enables the transformation of dislocation pile-ups into planar dislocation structures. Under the current diffraction conditions, $g = 200$ (g is the diffraction vector), the partial dislocations are not visible whereas the stacking faults associated with

Table 1
Evolution of the grain area fraction and the average size of the different types of dislocation substructures with true strain (see also Figs. 5, 6 and 9).

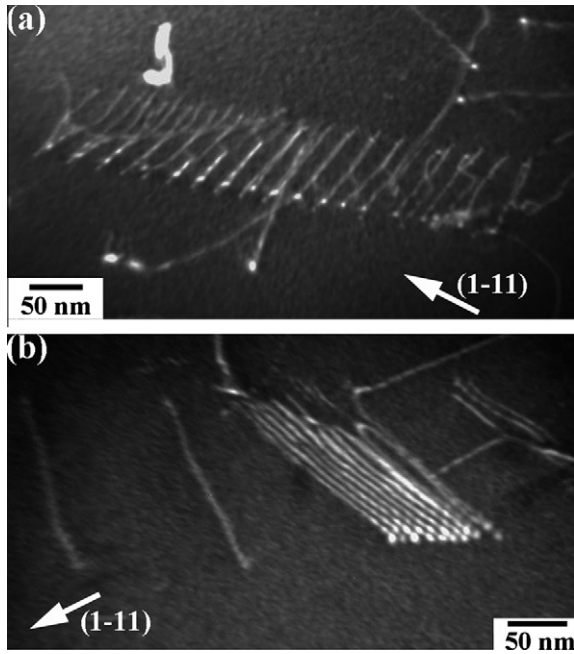| True strain	True stress (MPa)	Area fraction	Taylor lattice size (nm)	Area fraction	Cell size (nm)	Area fraction	Cell block size (nm)
0.1	710	$\sim 100\%$	450 ± 80	–	–	–	–
0.2	950	–	–	15%	195 ± 50	85%	270 ± 70
0.3	1150	–	–	10%	180 ± 40	90%	220 ± 50
0.57	1650	–	–	Not measured	110 ± 20	Not measured	Not measured

Fig. 2. Weak-beam TEM images of dislocation configurations in a sample deformed to 0.05 true strain/450 MPa: (a) dipole bundle lying parallel along the $(-11-1)$ plane, (b) multipole configurations of edge dislocations. Diffraction vectors are indicated by an arrow.

them are visible. Fig. 3c shows an area containing Lomer–Cottrell (LC) locks. These dislocation configurations are formed by the interaction of dissociated dislocations provided that the leading $\langle 112 \rangle$ partials attract one another. The dislocation product is a $\langle 110 \rangle$ sessile dislocation lying on $\{001\}$ planes. In particular, this figure reveals Lomer–Cottrell dislocations appearing as straight dislocations lying along the $[1-10]$ crystallographic direction and forming Lomer–Cottrell locks (labeled as LC1 and LC2). These locks act as strong barriers to dislocations with slip directions $[101]$ and $[10-1]$. Lomer–Cottrell locks are known to be one of the most important barriers to dislocation glide in stage II hardening of fcc metals [38–40].

3.2.2. Deformation stage: 0.1 true strain/710 MPa

The dislocation structure at this deformation stage is characterized by planar dislocation arrays formed by Taylor lattices and HDDWs (Figs. 4 and 5). Slip bands consisting of pile-up dislocations gliding along the primary slip system and crossing through the grain interior are visible (Fig. 4a). These slip bands contain different average dislocation densities indicating the localization of plasticity along the primary slip system. As secondary slip proceeds, such dislocation configurations transform into dense dislocation networks of planar dislocation arrays forming the so-called Taylor lattices [41] (Fig. 4b). In particular, this figure shows an example of a Taylor lattice formed by two non-coplanar slip systems. These dislocation structures are characteristic of metals with pronounced planar slip [41–43]. Fig. 4c shows an area containing HDDWs along the primary slip system nucleated at a grain boundary
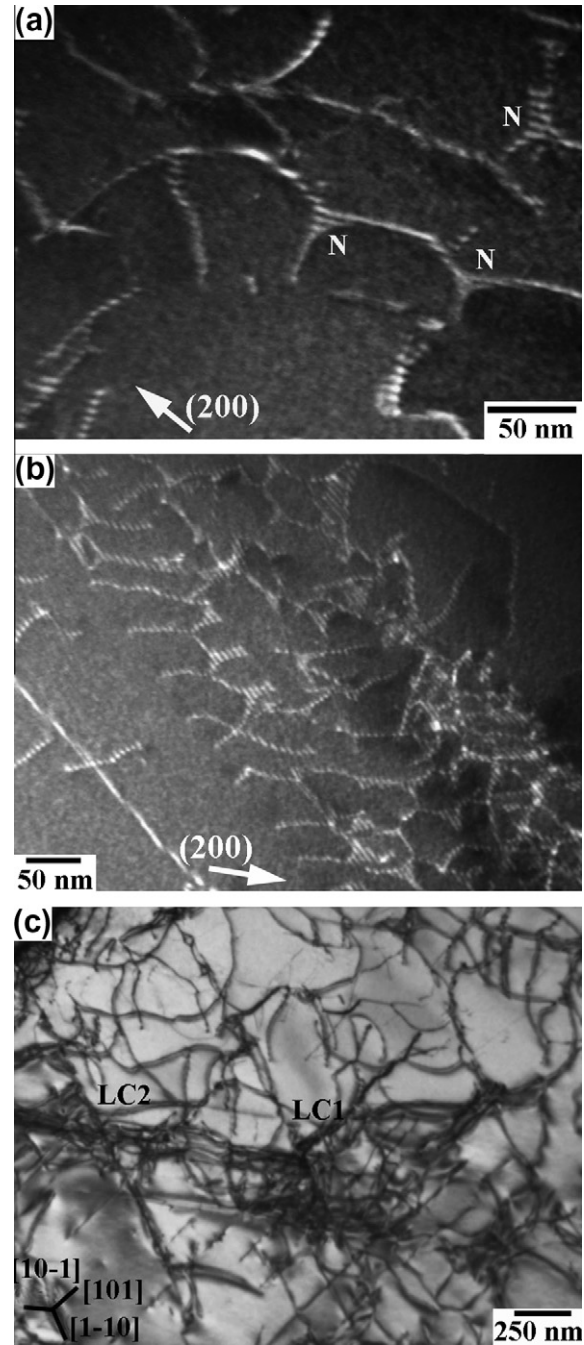

Fig. 3. Extended planar dislocation configurations in a sample deformed to 0.05 true strain/450 MPa: (a) dislocation nodes (N), (b) hexagonal dislocation networks. The stacking faults associated to the partial dislocations are visible. Diffraction vectors are indicated by an arrow. (c) Lomer–Cottrell locks (LC1 and LC2). Lomer–Cottrell dislocations appear as straight dislocations lying along the $[1-10]$ direction.

(GB). These structures are viewed in edge-on position with the $(-1-11)$ reflector parallel to the dislocation walls. The weak alternating contrast between adjacent volumes delimited by HDDWs indicates the small misorientation of the dislocation walls ($<1°$), as revealed by the corresponding diffraction pattern. The weak-beam TEM image of Fig. 4d reveals that HDDWs are formed by dense disloca-
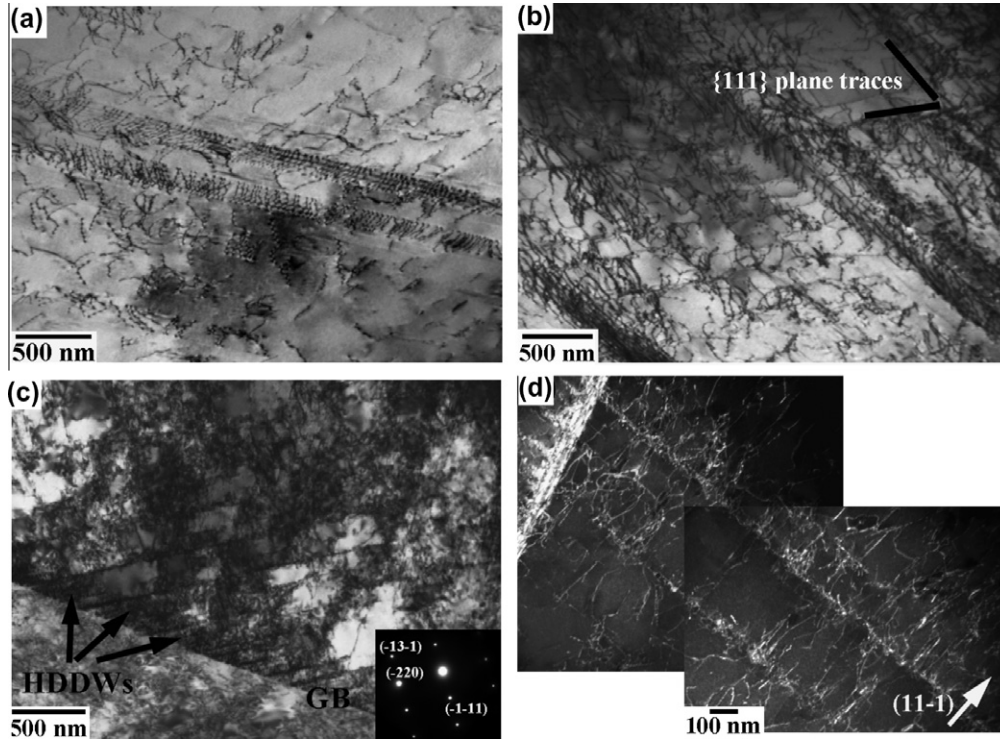
Fig. 4. Dislocation configurations in a sample deformed to 0.1 true strain/710 MPa: (a) slip bands consisting of pile-up dislocations gliding along the primary slip system and crossing through the grain interior, (b) Taylor lattices formed by two non-coplanar slip systems, (c) HDDWs formed along the primary slip system nucleated at a grain boundary (GB), (d) weak-beam TEM image of HDDWs at high magnification. Diffraction vector is indicated by an arrow.
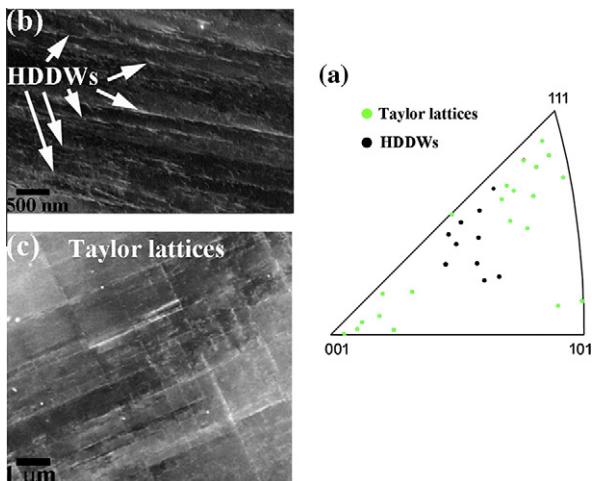

Fig. 5. (a) Inverse pole figure along the tensile axis direction showing experimental grain orientations of a sample deformed to 0.1 true strain/ 710 MPa (green dots: Taylor lattices; black dots: HDDWs), (b and c) ECCI images of HDDWs and Taylor lattices, respectively. (For interpretation of the references to color in this figure legend, the reader is referred to the web version of this article.)

tion sheets lying on the primary slip system. These dislocation structures are spaced between 100 and 300 nm.

The crystallographic orientation dependence of the dislocation patterns, namely, Taylor lattices and HDDWs, was investigated by combined EBSD and ECCI in 30 individual grains (Fig. 5). Fig. 5a shows the inverse pole figure along the tensile axis direction showing experimentally investigated grain orientations of a sample deformed to 0.1 true strain. Green and black dots correspond to Taylor lattices (green) and HDDWs (black), respectively. The crystal orientations of the grains analyzed represent the crystallographic texture of the material. HDDWs and Taylor lattices (Fig. 5b and c, respectively) are imaged by ECCI as dislocation configurations delimited by dense dislocation sheets which appear as bright straight compact layers due to the electron channeling mechanism and the Bragg diffraction conditions used to image the dislocation structures. Taylor lattices were the most frequently observed dislocation structures with an average size of 450 ± 80 nm. Apparent Taylor lattice sizes were measured from ECCI images and corrected values were then determined by means of a stereological correction considering the corresponding tilting conditions. HDDWs were mostly observed in grains favorably oriented to single slip. Those grains oriented closer to $\langle 1\,1\,1 \rangle$//TA directions develop a complex dislocation structure formed by HDDWs and Taylor lattices.

3.2.3. Deformation stage: 0.2 true strain/950 MPa

This deformation stage is characterized by the following features: the dislocation substructure consists of planar and wavy dislocation configurations with strong crystal orientation dependence. Further, deformation twinning is activated but at the present deformation stage its activity is

very low (twin area fraction is below 0.01). Specifically, Taylor lattices transform into cell blocks (CBs) and dislocation cells (DCs). CBs are dislocation structures delimited by HDDWs which are subdivided by dislocation walls
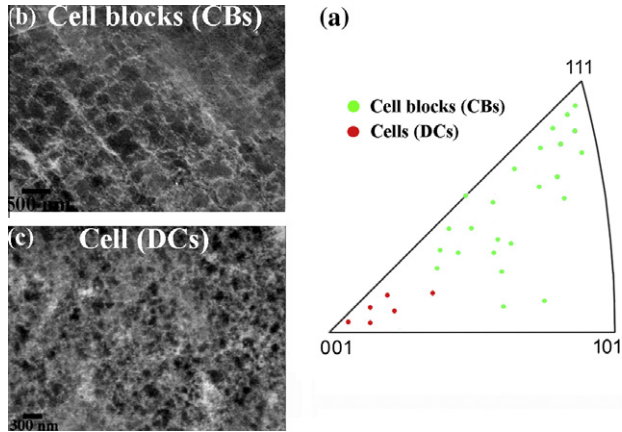

Fig. 6. (a) Inverse pole figure along the tensile axis direction showing experimental grain orientations of a sample deformed to 0.2 true strain/950 MPa (red dots: cells (DCs); green dots: cell blocks (CBs)), (b and c) ECCI images of CBs (b) and DCs (c), respectively. (For interpretation of the references to color in this figure legend, the reader is referred to the web version of this article.)
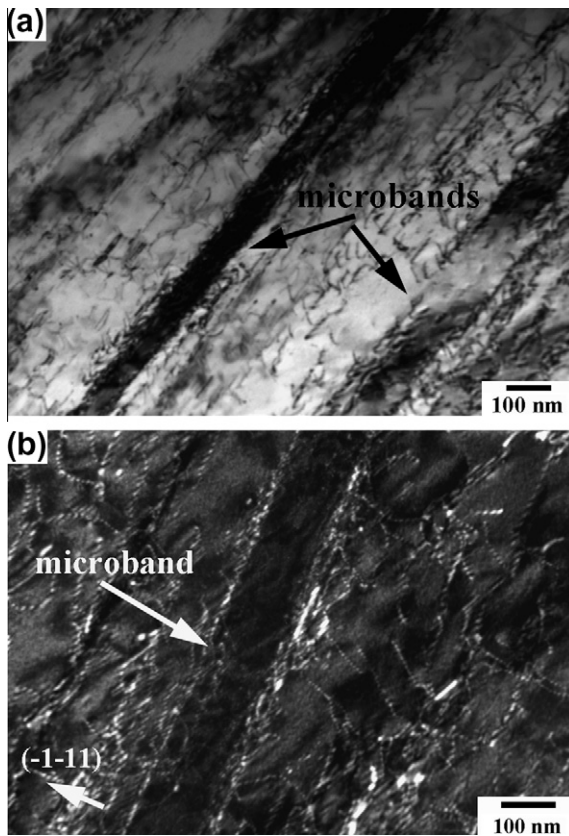

Fig. 7. (a) Bright-field TEM image of an area containing microbands in a sample deformed to 0.2 true strain/950 MPa, (b) weak-beam TEM image of a microband revealing details of the dislocation configuration. Diffraction vector is indicated by an arrow.

formed by statistical dislocation trapping (incidental dislocation boundaries [44]). These dislocation structures are imaged by ECCI as bright compact parallel layers (HDDWs) subdivided by finer bright layers (dislocation walls) (Fig. 6b). At the present strain level, ∼85% of the grains contain CBs with an average size of 270 ± 70 nm. The activation of wavy slip enables the formation of equiaxed DCs similar to those observed in medium-to high stacking fault energy metals [4,29,45,46]. These dislocation substructures are imaged by ECCI as bright globular structures with a sharp boundary contrast (Fig. 6c). The area fraction of grains containing cells is ∼15% and the average cell size is 195 ± 50 nm. Fig. 7a illustrates an area containing microbands. No detailed quantification was performed since the number of microbands observed at 0.2 true strain was very low. As the weak-beam TEM image of Fig. 7b reveals, microbands are thin dislocation configurations formed by a pair of dislocation sheets of ∼100 nm in thickness. The dislocation activity in the microband interior is very low compared to that in the matrix. This indicates a strong localization of deformation at the microband walls.

The crystallographic orientation dependence of the dislocation patterns, namely, cell blocks and cells, was investigated by combined EBSD and ECCI in 30 individual grains with a representative orientation distribution that matches the overall texture (Fig. 6a). This figure shows the inverse pole figure along the tensile axis direction showing the grain orientations that were studied in a sample deformed to 0.2 true strain. Green and red dots correspond to CBs (green) and DCs (red), respectively. The data indicate that cell pattering has strong crystal orientation dependence. Equiaxed cells are only developed in grains oriented close to $\langle 001 \rangle$//TA directions (Fig. 6c). The remaining grains analyzed contain a well-developed cell block structure (Fig. 6b). The shape of such structures depends on the number of active sip systems.

3.2.4. Deformation stage: 0.3 true strain/1150 MPa

The main characteristic of this deformation stage is the increasing twinning activity resulting in a well-defined twin

Fig. 8. Large view field ECCI image of deformed sample to 0.3 true strain/1150 MPa showing a multiple twin structure with dislocation substructures.
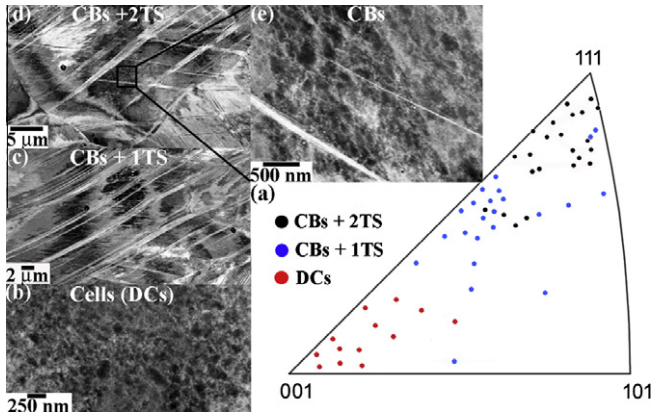
Fig. 9. (a) Inverse pole figure along the tensile axis direction showing experimental grain orientations of a sample deformed to 0.3 true strain/ 1150 MPa (red dots: cells (DCs); blue dots: cell blocks plus one twinning system (CBs + 1TS); black dots: cell blocks plus two twinning systems (CBs + 2TS)), (b e) ECCI images of corresponding dislocation and twin substructures. (For interpretation of the references to color in this figure legend, the reader is referred to the web version of this article.)
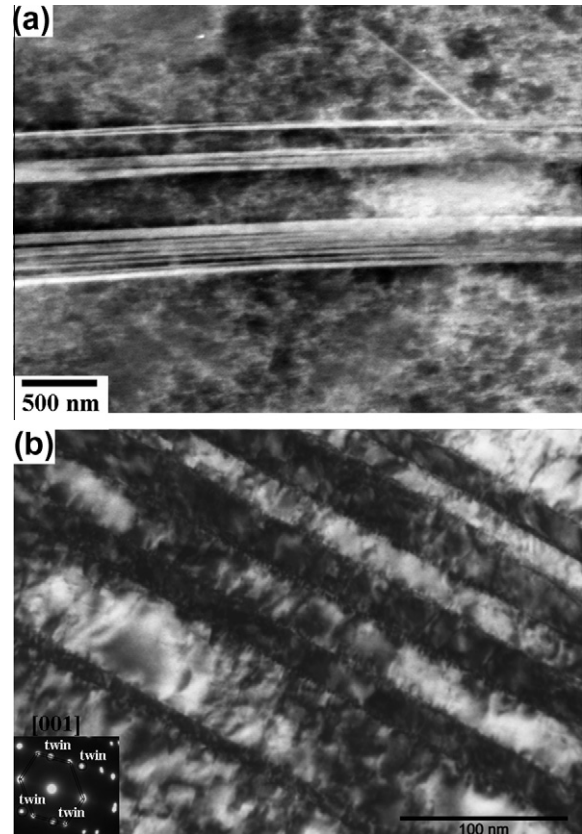

Fig. 10. (a) ECCI image of a bundle of twins in a sample deformed to 0.3 true strain/1150 MPa, (b) detail of a bundle of deformation twins showing single twins with nanometer thickness. Deformation wins are imaged edge-on. The BF-TEM image was obtained close to the zone axis [0 0 1]. Reflections from twins are indicated in the corresponding diffraction pattern.
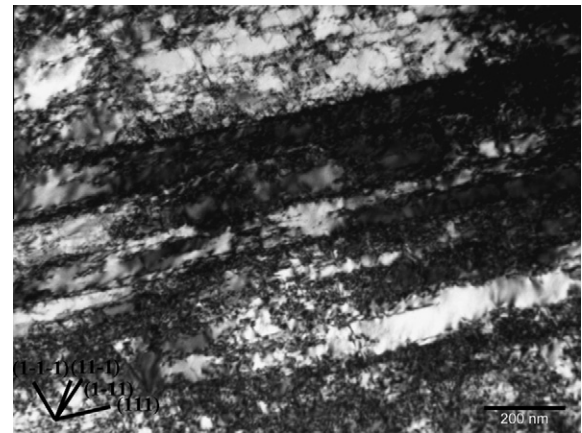

Fig. 11. TEM image of a grain oriented close to the [−3 7 9] crystallographic direction in a sample deformed to 0.3 true strain/1150 MPa. Microbands are formed along the {1 1 1} planes with the highest Schmid factors (−0.5: ⟨1 1 −1⟩ (1 1 1); −0.4: ⟨1 1 0⟩ (1 1 1)).

substructure (Fig. 8). At this deformation stage, ∼2/3 of the grains contain deformation twins that are active on several twinning systems. The grain orientation dependence of the deformation structure was analyzed by combined EBSD and ECCI in 60 individual grains (Fig. 9). The data reveal that we can systematically distinguish three types of grains. The first group consists of grains that are characterized by a dislocation cell structure with low deformation twinning activity (Fig. 9b). These grains contain an area fraction of ∼10% and are oriented close to ⟨0 0 1⟩//TA directions within an angular range of ∼15° (red dots in Fig. 9a). The average cell size in these grains is 180 ± 40 nm and their shapes depend on the number of slip systems activated. The closer the grain is oriented to ⟨0 0 1⟩//TA directions the more equiaxed is the cell shape. The second group assembles grains that contain combined dislocation and twin substructures formed by dislocation cell blocks and lamellar twin structures (Fig. 9c). The area fraction of these grains is ∼30%. They are oriented close to ⟨1 1 2⟩//TA directions within an angular range of ∼15° (blue dots in Fig. 9a). The third group contains grains which build up a complex deformed structure consisting of dislocation cell blocks and multiple-twin substructures (Fig. 9d and e). These grains, which are oriented close to ⟨1 1 1⟩//TA directions within an angular range of ∼15° (black dots in Fig. 9a), are the most frequent grains with an area fraction of ∼60%. At 0.3 true strain, the average cell block size in grains oriented close to ⟨1 1 1⟩//TA or ⟨1 1 2⟩//TA directions is 220 ± 50 nm. Deformation twins are typically arranged in bundles with thicknesses between 100 and 500 nm (Fig. 10a). These bundles are formed by thin deformation twins with thicknesses ranged between 10 and 50 nm (Fig. 10b). This twin configuration is typical of high-Mn steels [4,8,17,27]. ECCI and TEM observations reveal that at 0.3 true strain, the number of microbands remains very low. Fig. 11 shows an example of an area con-

taining microbands. The grain is oriented close to the [−3 7 9] crystallographic direction. Microbands are formed along {1 1 1} planes which correspond to the slip plane with the highest Schmid factors (−0.5: ⟨1 1 −1⟩ (1 1 1); −0.4:

$\langle 1\,{-}1\,0 \rangle$ $(1\,1\,1)$). This image reveals that most of the deformation activity is localized along these slip systems.

4. Discussion

4.1. Dislocation substructure

The FeMnAlC steel exhibits a pronounced evolution in the dislocation configuration upon deformation. We attribute this to the role of solute carbon on dislocation maneuvers. At the early stages of deformation (<0.1 true strain), the formation of dislocation configurations such as pileups, multipoles, HDDWs and Taylor lattices indicate strong planar slip character. HDDWs are mainly observed in grains oriented favorably to coplanar or single slip whereas multiple-slip tends to form a homogeneous Taylor lattice structure. Planar slip is promoted in fcc metals by decreasing the stacking fault energy (SFE), increasing the frictional stress due to solute content and the occurrence of short range ordering (SRO) [47,48]. In the FeMnAlC steel studied here, the addition of aluminum and carbon may significantly increase the SFE. To evaluate this effect, we have estimated the SFE at room temperature by means of a modified Olson–Cohen thermodynamical model [14,49]. This approach has been widely applied to high-Mn alloys [3,6,9,15,18,50,51]. In particular, Jin et al. [9] have recently shown that in the FeMnAlC system, the thermodynamical approach provides similar SFEs than those obtained by conventional X-ray diffraction methods. Using thermodynamical data available for the FeMnAlC system [3,9,14,50,52], we estimate a SFE of 63 mJ m^{-2} for the Fe–30.5Mn–2.1Al–1.2C (wt.%) alloy. Magnetic effects were not considered in the present calculation because austenite is paramagnetic at room temperature [53]. This value is close to the reported SFE of 50 mJ m^{-2} in a Fe–31Mn–2.7Al–1.0C (wt.%) alloy [21]. The estimated SFE is similar to that of metals exhibiting non-planar slip character, such as copper [54]. Accordingly, the planar slip character in the alloy studied here cannot be ascribed to the SFE. Detailed observations of TEM diffraction patterns did not reveal diffuse scattering, as would be indicative of short range ordering. We therefore conclude that the planar slip character in the present alloy can be mainly associated to frictional stress effects. Among the different solute species in the present alloy, namely, manganese, aluminum and carbon, the latter provides the strongest dislocation–solute interaction [55]. We can therefore expect a frictional stress effect due to the high carbon content of the present alloy (1.2 wt.%). High frictional stresses have been already reported in high-Mn steels containing the half amount of carbon [56].

With further deformation, 0.2 true strain, wavy slip is remarkably observed, leading to the formation of characteristic dislocation configurations such as cells (DCs) and cell blocks (CBs). DCs are build up in grains when a high number of slip planes are activated and dislocation cross-slip is significantly enabled [43,57], namely, in grains oriented close to $\langle 0\,0\,1 \rangle$//TA directions. Grains containing a limited number of active slip systems tend to form CBs. In particular, multiple-slip enables the formation of non-crystallographic dislocation boundaries (i.e. grains oriented close to $\langle 1\,1\,1 \rangle$//TA directions) whereas single or coplanar slip tends to produce planar boundaries on crystallographic slip planes (crystallographic dislocation boundaries) [58]. DCs and CBs have been reported in tensile deformed medium-to-high stacking fault energy metals such as copper and aluminum [54,59]. However, the macroscopic stress required to form such dislocation structures in the present FeMnAlC steel, 950 MPa, is much higher than that observed in medium-to-high stacking fault energy metals with similar average grain sizes ($\sim$100 MPa [60]).

At the present low deformation temperature (room temperature), cell formation is controlled by dislocation cross-slip due to the low activity of dislocation climb. Cross-slip plays an important role in the cell formation through the re-arrangement of screw dislocations in terms of the activation of secondary slip and annihilation of screw dislocations of opposite sign. The localized maneuvers of partial dislocations to transfer dislocation screw segments from one plane to another depend on the SFE [61,62]. However, as the SFE of the alloy studied here is high ($\sim$60 mJ m^{-2}), this means that there is another microstructure parameter having a strong influence on the cross-slip frequency. As the FeMnAlC steel is austenitic, i.e. fcc, we assume the Fridel–Escaig model of dislocation cross-slip to be applied [63,64]. This model describes the dislocation configuration required for a dissociated screw dislocation to cross-slip into a $\{1\,1\,1\}$ slip plane. According to the Fridel–Escaig model, this event is determined by the energy required for the recombination or constriction of the two Shockley partials into the cross-slip plane, which is strongly dependent on the stress component acting on the edge parts of the partials. As these partials may interact with a surrounding solute atom field, we therefore expect a significant influence of the carbon field on the constriction energy of cross-slip in the FeMnAlC alloy. Andrews et al. have recently calculated the dependence of the constriction energy on size misfit, modulus mismatch and solute concentration for a screw dislocation in an fcc metal in the presence of a solute field, in particular carbon [65]. The results show that the dislocation–solute field interaction has a strong positive contribution to the total constriction energy. In other words, the presence of a carbon field strongly hinders dislocation cross-slip in fcc metals. In the present FeMnAlC alloy, the high carbon content in solid solution (1.2 wt.%) delays the formation of dislocation structures assisted by cross-slip and shifts them to high macroscopic stress levels. It is worth mentioning that this effect is strongly dependent on the carbon content in solid solution. In particular, we have not observed such effect in a tensile deformed Fe–22Mn–0.6C (wt.%) steel where cells are formed at a lower stress level than in the FeMnAlC steel ($\sim$300 MPa [4]).

4.2. Strain hardening

The strain hardening behavior of the Fe–30.5Mn–2.1Al–1.2C (wt.%) alloy in solid solution state is characterized by a multiple-stage behavior. In contrast, conventional high-Mn steels containing average grain sizes similar to that obtained in the alloy studied here (50 µm) typically exhibit a single hardening stage associated with a high overall strain hardening (the so-called twinning-induced plasticity, TWIP, effect) [4,6,8,9,12,23]. It is worth pointing out that variations in the strain hardening behavior due to grain size [8,23] or strain rate effects can be found [66]. Stage A hardening is characterized by a decrease in the strain hardening rate. TEM observations reveal that this stage contains dislocation configurations similar to those found in stage II hardening of low stacking fault energy fcc metals, namely, multipoles, dipoles, hexagonal networks and Lomer–Cottrell locks. The low activity of cross-slip suggests that dynamic recovery processes such as annihilation of screw dislocations are limited. Accordingly, this stage can be associated to dislocation hardening, mainly by Lomer–Cottrell locks, and reduced dynamic recovery. The microstructure observations indicate that stage B is associated to dislocation substructure hardening via Taylor lattices. This hardening mechanism is typically observed in materials with pronounced planar slip behavior [43,45,67]. The value of the strain hardening coefficient observed in this regime, $G/27$, is remarkably higher than the typical value of $G/200$ observed for multiple slip in common fcc metals [33,40]. However, it is similar to the hardening coefficient ascribed to dislocation substructure hardening found in FeMnC alloys ($G/20$–$G/40$ [4,68,69]). With further deformation, the dislocation substructure evolves from Taylor lattices to cells (DCs) and cell blocks (CBs). The limited refinement of the size of the dislocation substructure and the significant activation of dislocation cross-slip lead to a decrease in the strain hardening, stage C.

Fig. 12 shows the variation of the average size of dislocation substructures, namely, Taylor lattices and CBs (white dots), and DCs (white squares), with resolved flow stress, τ. Error bars of the average size of dislocation substructures obtained from the statistical treatment of the data are included. We use the microstructure parameters shown in Table 1. For comparison, we also include the evolution of the average cell sizes upon tensile deformation of a Fe–22Mn–0.6C (wt.%) alloy containing a similar average grain size than the alloy studied here [4]. τ was obtained from σ/M, where σ is the macroscopic applied stress and M is the corresponding Taylor factor estimated from the texture ($M = 2.44$ for cell-forming crystals, i.e. grains oriented $\langle 0\,0\,1 \rangle$//TA directions, and M is ranged between 2.8 and 3.1 for non cell-forming crystals). This figure reveals that both types of dislocation substructures, viz. Taylor lattices and CBs, and DCs follow a relationship:

$$\tau = GKb/D \qquad (1)$$

where τ is the resolved flow stress, G is the shear modulus, K is a constant, b is the magnitude of the Burgers vector and D is the dislocation substructure size. This is a widely observed empirical relationship that has been well established and confirmed in the framework of the mesh-length theory of work hardening [43,67]. Using $b = 2.5 \times 10^{-10}$ m [70] and $G = 70$ GPa [32], we obtain a value of the constant K of 3.6 for Taylor lattices and CBs, $K_{TLs+CBs}$, and 3.8 for DCs, K_{DCs}. Interestingly, these values are very close to that obtained for DCs in the Fe–22Mn–0.6C alloy, $K_{DCs} = 3.7$. Two important conclusions can be drawn from these findings. First, the sizes of the different types of dislocation substructures present in the FeMnAlC steel, namely, Taylor lattices, CBs, and DCs follow the same stress dependence. Second, this stress dependence is practically the same as that obtained for cell-forming crystals free of twins in a Fe–22Mn–0.6C steel. These results reveal that the specific dislocation mechanisms involved in the formation of the different dislocation substructures, in particular, dislocation cross-slip, determine the type of dislocation substructure, viz. Taylor lattices, CBs or DCs. The size of such dislocation substructures scales inversely with the applied resolved stress.

In order to yield a better understanding of the influence of the dislocation substructure on strain hardening, we have evaluated its contribution to the flow stress, $\Delta\sigma$, at different strain levels, specifically, between 0.1 and 0.3 true strain, by means of Eq. (1) and the relationship $\sigma = M\tau$, where M is the Taylor factor. We use the microstructure parameters shown in Table 1, the values of M, b and G used in Fig. 12, and the constants K previously calculated. Fig. 13 shows the calculated stresses from Eq. (1) together with the overall flow stress. Error bars of the stresses calculated from the statistical distribution of the dislocation substructure size, D, is included. This figure reveals that the calculated stresses follow the same evolution with strain as the experimental flow stress. The difference in the absolute stress values, σ–$\Delta\sigma$, is constant. We ascribe this stress, $\sim$300 MPa, to the frictional stress. We expect a value of the frictional stress close the yield stress (420 MPa) in the
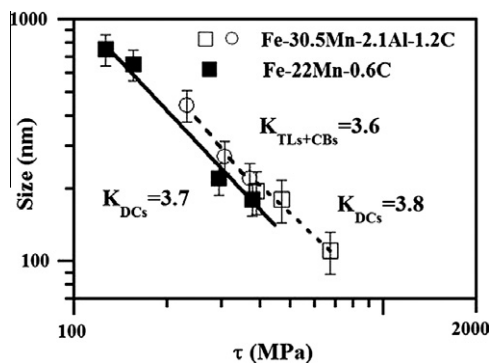

Fig. 12. Variation of the average size of dislocation substructures with flow stress in a Fe–30.5Mn–2.1Al–1.2C (wt.%) steel (white dots: Taylor lattices (TLs) and cell blocks (CBs); white squares: cells (DCs)) and a Fe–22Mn–0.6C (wt.%) steel (black squares: cells (DCs)). The constant K is calculated from the relationship $\tau = KGb/D$ (see also Figs. 5, 6 and 9).
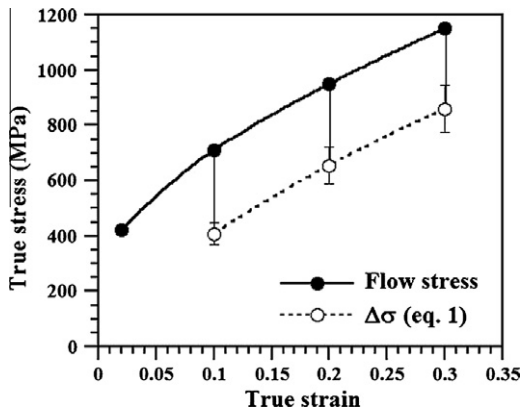
Fig. 13. Contribution of the dislocation substructure to the flow stress calculated from Eq. (1) (white dots) and overall flow stress (black dots) in the strain range 0.1–0.3 true strain (see also Figs. 5, 6 and 9).

present alloy due to the large grain size (50 μm). This analysis indicates that within the strain regime between 0.1 and 0.3 true strain, i.e. hardening stages B–C, the main structural parameter that determines the flow stress and the strain hardening is the size of the dislocation substructure.

With further straining, the development of a twin substructure results in a further decrease of the dislocation mean free path (MFP) leading to stages D–E hardening. Twin boundaries act as strong obstacles to dislocation motion serving as efficient sites for dislocation accumulation. The contribution of twinning to hardening can be described by [4,71]:

$$\Delta\sigma_{twinning} = K_{H-P}/(\lambda_{twin})^{1/2} \qquad (2)$$

where K_{H-P} is a constant and λ_{twin} is the average twin spacing. The crystallographic orientation dependence of the twin substructure is similar to that found in a tensile deformed Fe–22Mn–0.6C (wt.%) alloy [4]: grains with a highly favorable (multiple twin substructure) or unfavorable orientation (no twin substructure) for twinning follow Schmid's law with respect to the macroscopic stress state. The rest of the crystals develop a lamellar twin substructure. These crystals exhibit deviations from Schmid's law which are associated to local stress concentrations at grain boundaries [13].

4.3. Deformation localization: HDDWs and microbands

We observe that the Fe–30.5Mn–2.1Al–1.2C (wt.%) alloy develops dislocation configurations upon straining that are characteristic of deformation localization phenomena, such as HDDWs and microbands (Figs. 4c and d, 5b and 7). These dislocation arrangements are characterized by a high dislocation activity along the primary slip system resulting in parallel dense dislocation arrays containing low dislocation densities in their interiors. As Fig. 5 shows, these dislocation configurations are mainly formed in grains oriented favorably to single or coplanar slip. Under the current tensile deformation, a typical α-fiber, character-

ized by two strong texture components, namely, ⟨1 1 1⟩//TA and ⟨0 0 1⟩//TA, is formed. Multiple slip is activated in these orientations and, hence, the number of grains containing HDDWs and microbands is low, in agreement with TEM and ECCI observations. Recently, it was proposed that microbanding can account for the good combination of strength and ductility in FeMnAlC steels [3,25,26] (the so-called microband-induced plasticity, MBIP). Yoo et al. have reported the formation of Taylor lattices, deformation bands and microbands upon tensile deformation in a Fe–28Mn–10Al–1.0C (wt.%) steel in solid solution state [3,25]. Based on their TEM observations, these authors attributed the high strain hardening to the formation of deformation bands and microbands. As the previous section shows, the FeMnAlC steel studied here exhibits a high strain hardening due to its specific dislocation substructure, namely, Taylor lattices, dislocation cells and cell blocks, and not due to microbands. In the present case, due to texture effects, microbanding is not favored during tensile deformation and, hence, plays no role in strain hardening. Also, from a more general point of view, we believe that microbanding plays no substantial role in strain hardening in FeMnAlC steels during tensile deformation: As Figs. 7 and 11 reveal, microbands are formed as a result of intense plastic localization on single or coplanar slip. Dislocation activity on secondary non-coplanar slip systems is limited. Accordingly, we expect from such highly localized microstructure a softening instead of a hardening effect.

4.4. Alloy design of high-Mn steels

In this section we compare the mechanical properties (strength/elongation) of the present FeMnAlC steel to those reported in similar high-Mn steel grades. We only focus on room temperature behavior and the solid solution state. Fig. 14 shows the plot of ultimate tensile strength (UTS) vs. elongation of several high-Mn steel grades obtained from engineering stress–strain curves [1,3,4,6,8,9,18,23,25,72,73]. We have classified the steel grades into medium Mn content, referred to as M–Mn,
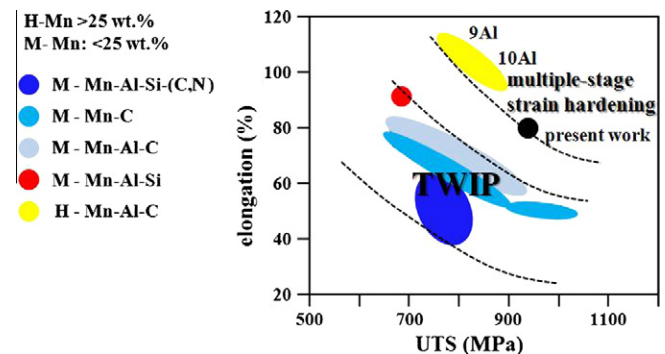

Fig. 14. Ultimate tensile stress (MPa) vs. elongation chart for several high-Mn steel grades. M–Mn: steels with Mn content lower than 25 wt.% Mn; H–Mn: steels with Mn content higher than 25 wt.% Mn. TWIP: twinning-induced-plasticity effect. Chemical composition in wt.%.

as those steels with a Mn content below 25 wt.%, and high Mn content, referred to as H–Mn, as those steels with a Mn content above 25 wt.% Mn. We analyzed results from four M–Mn grades: M–Mn–C [8,9,18,73], M–Mn–Al–C [1,5,6] and M–Mn–Al–Si+(C,N) [4,23,72]. The strain hardening behavior of these steels exhibits the typical twinning-induced plasticity (TWIP) effect, namely, microstructure refinement by deformation twinning. Twin spacing is the key microstructural parameter due to the activation of deformation twinning at low-to-intermediate macroscopic stress values [74,75]. Accordingly, twinning kinetics determine the mechanical properties.

The present H–Mn–Al–C steel presents a superior combination of strength and ductility due to its multiple-stage strain hardening behavior associated to dislocation substructure refinement and subsequent activation of deformation twinning after reaching high stress levels. As the twinning stress, $\sigma_{twinning}$, scales with the SFE [76]:

$$\sigma_{twinning} \sim \gamma/b \tag{3}$$

where γ is the SFE and b is the magnitude of the Burgers vector, a considerable high macroscopic stress is required to promote twinning in the present alloy. This agrees with the outstanding mechanical properties obtained in H–Mn–Al–C alloys with high Al content (9–10 wt.%) [3,25]. These results confirm that the H–Mn–Al–C grade is a promising high performance steel. The key features of the excellent strain hardening behavior of the present steel are as follows. First, the development of a fine dislocation substructure with nanometer size: this is ascribed to the role of carbon solute on dislocation cross-slip. Due to the high carbon content of the H–Mn–Al–C system ($\sim$1 wt.%), cross-slip is strongly impeded. As a consequence, its frequency increases with the applied stress, resulting in a gradual transition in the type of dislocation configuration from planar (Taylor lattices) to wavy (cells, cell blocks). This dislocation transition is key to minimizing damage mechanisms triggered by local stress concentrations at grain boundaries provided by dense planar dislocation configurations. Second, the development of a twin substructure at intermediate deformation levels results in a further microstructure refinement (TWIP effect). The good mechanical compatibility between dislocation slip and the evolving twin interfaces results in a critical stress required to transfer plastic deformation across the twin bundle, $\tau_{t-transfer}$, which is only dependent on the shear modulus, G, and twin thickness t:

$$\tau_{t-transfer} \sim Gb/t \tag{4}$$

where b is the magnitude of the Burgers vector. This stress is higher than that required to transfer plasticity across a dislocation boundary with low misorientation:

$$\tau_{db-transfer} \sim Gb(\theta/Db)^{1/2} \tag{5}$$

where D is the dislocation substructure size and θ is the misorientation angle [77,78]. Accordingly, the strength of the twin interface is higher than that of a dislocation boundary against dislocation glide. In other words, the effect of twinning on the flow stress is higher than that of dislocation substructure refinement. The present study indicates that multiple-stage strain hardening due to size refinement of the dislocation substructure and the subsequent activation of deformation twinning, which leads to a steady increase of strain hardening, promotes an enhanced combination of strength and ductility.

5. Conclusions

We investigated the underlying kinetics of the deformation structure evolution and its contribution to the strain hardening of a Fe–30.5Mn–2.1Al–1.2C (wt.%) steel during tensile deformation by means of TEM and ECCI combined with EBSD. The following conclusions are drawn:

– The present steel exhibits a superior combination of strength and ductility (ultimate tensile strength of 1.6 GPa and elongation to failure of 55%) due to the multiple-stage strain hardening behavior associated to dislocation substructure refinement and subsequent activation of deformation twinning, which leads to a steadily increase of the strain hardening.

– The early hardening stage is fully determined by the size of the dislocation substructure, namely, Taylor lattices, cell blocks and dislocation cells. We do not observe the so-called microband-induced plasticity (MBIP) effect. In the present case, due to texture effects, microbanding is not favored during tensile deformation and, hence, plays no role in strain hardening. We further suggest that due to the highly localized nature of microbands, they should rather produce a softening instead of a hardening effect.

– The characterization of dislocation substructure evolution reveals a strong influence of carbon solute on the evolving dislocation substructure. We attribute this effect to the role of carbon on dislocation cross-slip. Due to the strong impediment of cross-slip, its frequency increases with the applied stress, resulting in a gradual transition in the type of dislocation configuration from planar (Taylor lattices) to wavy (cells, cell blocks).

– The specific dislocation mechanisms involved in the formation of the different dislocation substructures, in particular, dislocation cross-slip, determine the resulting type of dislocation substructure, viz. Taylor lattices, cell blocks or cells. The size of such dislocation substructures scales inversely with the applied resolved stress.

References

[1] Grässel O, Krüger L, Frommeyer G, Meyer LW. Int J Plast 2000;16:1391.
[2] Scott C, Allain S, Faral M, Guelton N. Rev Metall 2006;103:293.
[3] Yoo JD, Park K-T. Mater Sci Eng A 2008;496:417.
[4] Gutierrez-Urrutia I, Raabe D. Acta Mater 2011;59:6449.
[5] Kim J-K, Chen L, Kim H-S, Kim S-K, Estrin Y, De Cooman BC. Metall Mater Trans A 2009;40A:3147.
[6] Curtze S, Kuokkala V-T. Acta Mater 2010;58:5129.
[7] Idrissi H, Renard K, Schryvers D, Jacques PJ. Scripta Mater 2010;63:961.
[8] Bouaziz O, Allain S, Scott CP, Cugy P, Barbier D. Current Opinion Solid State Mater Sci 2011;15:141.
[9] Jin J-E, Lee Y-K. Acta Mater 2012;60:1680.
[10] Lee S-J, Kim J, Kane SN, De Cooman BC. Acta Mater 2011;59:6809.
[11] Koyama M, Sawaguchi T, Lee T, Lee CS, Tsuzaki K. Mater Sci Eng A 2011;528:7310.
[12] Allain S, Chateau JP, Bouaziz O. Mater Sci Eng A 2004;387–389:143.
[13] Gutierrez-Urrutia I, Zaefferer S, Raabe D. Mater Sci Eng A 2010;527:3552.
[14] Dumay A, Chateau JP, Allain S, Migot S, Bouaziz O. Mater Sci Eng A 2008;483–484:184.
[15] Saeed-Akbari A, Imlau J, Prahl U, Bleck W. Metall Mater Trans A 2009;40A:3076.
[16] Shiekhelsouk MN, Favier V, Inal K, Cherkaoui M. Int J Plast 2009;25:105.
[17] Idrissi H, Renard K, Ryelandt L, Schryvers D, Jacques PJ. Acta Mater 2010;58:2464.
[18] Park K-T, Jin KG, Han SH, Hwang SW, Choi K, Lee CS. Mater Sci Eng A 2010;527:3651.
[19] Dastur YN, Leslie WC. Metall Trans A 1981;12A:749.
[20] Zuidema BK, Subramanyam DK, Leslie WC. Metall Trans A 1987;18A:1629.
[21] Shun T, Wan CM, Byrne JG. Acta Metall Mater 1992;40:3407.
[22] Saeed-Akbari A, Mosecker L, Schwedt A, Bleck W. Metall Mater Trans A 2012;43A:1688.
[23] Gutierrez-Urrutia I, Raabe D. Scripta Mater 2012;66:992.
[24] Dancette S, Delannay L, Renard K, Melchior MA, Jacques PJ. Acta Mater 2012;60:215.
[25] Yoo JD, Hwang SW, Park K-T. Metall Mater Trans A 2009;40A:1520.
[26] Park K-T, Kim G, Kim SK, Lee SW, Hwang SW, Lee CS. Metal Mater Int 2010;16:1.
[27] Gutierrez-Urrutia I, Zaefferer S, Raabe D. Scripta Mater 2009;61:737.
[28] Gutierrez-Urrutia I, Raabe D. Scripta Mater 2012;66:343.
[29] Gutierrez-Urrutia I, Raabe D. Mater Sci Forum 2012;702–703:523.
[30] Eisenlohr A, Gutierrez-Urrutia I, Raabe D. Acta Mater 2012;60:3994.
[31] Zhang ZF, Wang ZG. Prog Mater Sci 2008;53:1025.
[32] Kim J, Lee SJ, De Cooman BC. The stacking fault energy of TWIP steels. Seoul: HMnS2011; 2011.
[33] Kocks UF, Mecking H. Prog Mater Sci 2003;48:171.
[34] Pande CS, Hazzledine PM. Philos Mag 1971;24:1039.
[35] Steffens T, Schwink C, Korner A, Karnthaler HP. Philos Mag A 1987;56:161.
[36] Feaugas X. Acta Mater 1999;47:3617.
[37] Jackson PJ. Prog Mater Sci 1985;29:139.
[38] Nabarro FRN. Theory of crystal dislocations. Oxford: Oxford University Press; 1967.
[39] Hirth JP, Lothe J. Theory of dislocations. New York: McGraw-Hill; 1968.
[40] Nabarro FRN, Basinski ZS, Holt DB. Adv Phys 1964;13:193.
[41] Hughes DA. Acta Metall Mater 1993;41:1421.
[42] Karaman I, Sehitoglu H, Maier HJ, Chumlyakov YI. Acta Mater 2001;49:3919.
[43] Kuhlmann-Wilsdorf D. Mater Sci Eng A 1989;113:1.
[44] Hughes DA, Hansen N, Bammann DJ. Scripta Mater 2003;48:147.
[45] Bay B, Hansen N, Hughes DA, Kuhlmann-Wilsdorf D. Acta Metall Mater 1992;40:205.
[46] Huang X. Scripta Mater 1998;38:1697.
[47] Gerold V, Karnthaler HP. Acta Metall 1989;37:2177.
[48] Hong SI, Laird C. Acta Mater 1990;38:1581.
[49] Allain S, Chateau JP, Bouaziz O, Migot S, Guelton N. Mater Sci Eng A 2004;387–389:158.
[50] Lee Y-K, Choi C-S. Metall Mater Trans A 2000;31A:355.
[51] Nakano J, Jacques PJ. CALPHAD 2010;34:167.
[52] Olson GB, Cohen M. Metall Trans A 1976;7A:1897.
[53] Huang W. Calphad 1989;13:243.
[54] Heino P, Perondi L, Kaski K, Ristolainen E. Phys Rev B 1999;60:14625.
[55] Bhadeshia HKDH, Honeycombe R. Steels: microstructure and properties. Oxford: Elsevier; 2006.
[56] Sevillano JG. Scripta Mater 2009;60:336.
[57] Bay B, Hansen N, Hughes DA, Kuhlmann-Wilsdorf D. Acta Metall Mater 1992;40:205.
[58] Winther G, Jensen DJ, Hansen N. Acta Mater 1997;45:5059.
[59] Schulthess TC, Turchi PEA, Gonis A, Nieh TG. Acta Mater 1998;46:2215.
[60] Kocks UF, Mecking H. Prog Mater Sci 2003;48:171.
[61] Hirth JP, Lothe J. Theory of dislocations. Chichester: Wiley; 1982.
[62] Jackson PJ. Prog Mater Sci 1985;29:139.
[63] Püschl W. Prog Mater Sci 2002;47:415.
[64] Bonneville J, Escaig B. Acta Metall 1979;27:1477.
[65] Andrews SD, Sehitoglu H, Karaman I. J Appl Phys 2000;87:2194.
[66] Rodriguez P. Metall Mater Trans A 2004;35A:2697.
[67] Kuhlmann-Wilsdorf D. Philos Mag A 1999;79:955.
[68] Canadinc D, Sehitoglu H, Maier HJ, Chumlyakov YI. Acta Mater 2005;53:1831.
[69] Canadinc D, Sehitoglu H, Maier HJ. Mater Sci Eng A 2007;454–455:662.
[70] Bouaziz O, Allain S, Scott C. Scripta Mater 2008;58:484.
[71] Asgari S, El-Danaf E, Kalidindi SR, Doherty RD. Metall Mater Trans A 1997;28A:1781.
[72] Huang BX, Wang XD, Wang L, Rong YH. Metall Mater Trans A 2007;39A:717.
[73] Jin J-E, Lee Y-K. Mater Sci Eng A 2009;527:157.
[74] Lu L, Sui ML, Lu K. Science 2000;287:1463.
[75] Yan FK, Liu GZ, Tao NR, Lu K. Acta Mater 2012;60:1059.
[76] Christian JW, Mahajan S. Prog Mater Sci 1995;39:1.
[77] Hughes DA, Hansen N. Acta Mater 2000;48:2985.
[78] Liu B, Raabe D, Eisenlohr P, Roters F, Arsenlis A, Hommes G. Acta Mater 2011;59:7125.